Electronic Supplementary Material (ESI) for Dalton Transactions.

SUPPORTING INFORMATION

Tuning the slow magnetic relaxation with the substituents in anilate bridged bis(dysprosium) complexes

Fabio Manna,[a,b,c] Mariangela Oggianu,[a,c] José Ramón Galán-Mascarós,[d,e] Flavia Pop,[b] Boris Le Guennic,[f] Maria Laura Mercuri[a,c]* and Narcis Avarvari[b]*

[a]*Dipartimento di Scienze Chimiche e Geologiche, Università degli Studi di Cagliari, I-09042 Monserrato, Italy. E-mail: mercuri@unica.it*

[b] *Univ Angers, CNRS, MOLTECH-ANJOU, SFR MATRIX, F-49000 Angers, France. E-mail: narcis.avarvari@univ-angers.fr*

[c] *INSTM, Via Giuseppe Giusti, 9, 50121 Firenze, Italy*

[d]*Institute of Chemical Research of Catalonia (ICIQ), The Barcelona Institute of Science and Technology (BIST), Av. Països Catalans 16, E-43007 Tarragona, Spain*

[e]*ICREA, Passeig Lluis Companys, 23, Barcelona 08010, Spain*

[f] *Univ Rennes, CNRS, ISCR (Institut des Sciences Chimiques de Rennes) – UMR 6226, F-35000 Rennes, France*

Contents

Crystallography and Thermal Analysis 3
Figure S1 3
Figure S2 4
Figure S3 4
Figure S4 5
Figure S5 5
Figure S6 6
Figure S7 6
Figure S8 7

Figure S9 7
IR and UV-Vis spectroscopy 8
Figure S10 8
Figure S11 9
Cyclic voltammetry measurements 11
Figure S13 11
Figure S14 12
Figure S15 13
Magnetic measurements 14
Figure S16 14
Figure S17 15
NMR characterization 16
Figure S18 16
Figure S19 17

Crystallography and Thermal Analysis

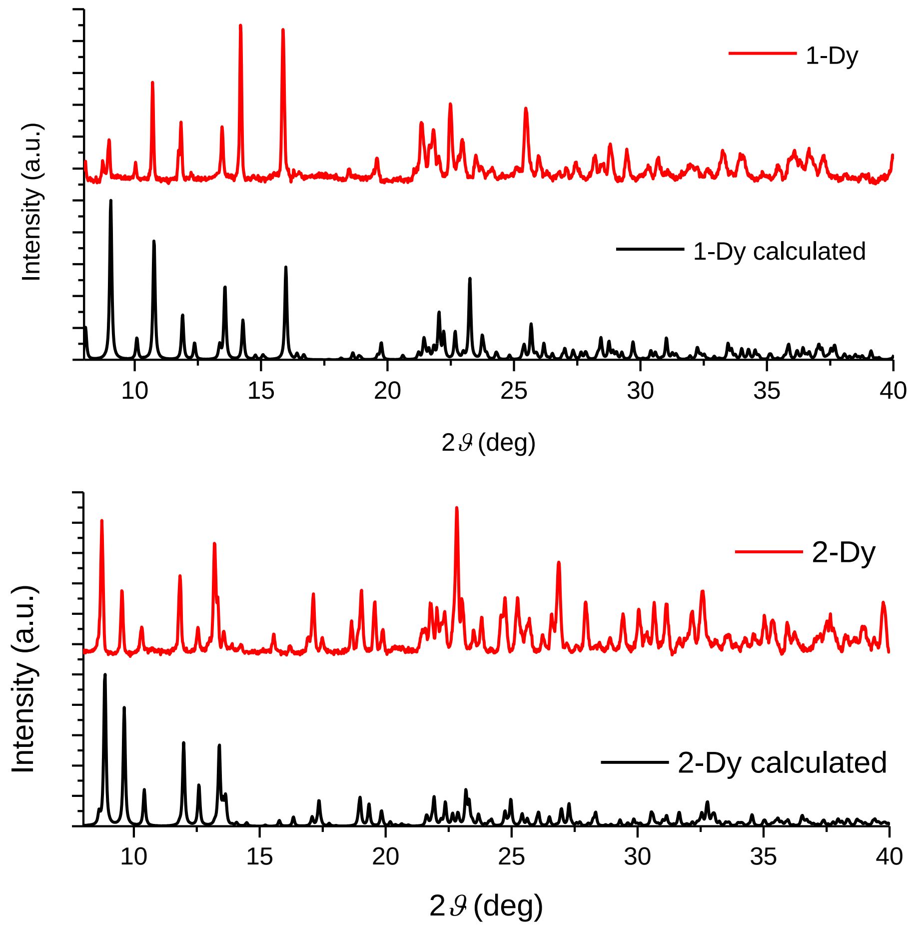

Fig. S1 PXRD experimental (top, red) and calculated (bottom, black) for **1Dy** and **2Dy**.

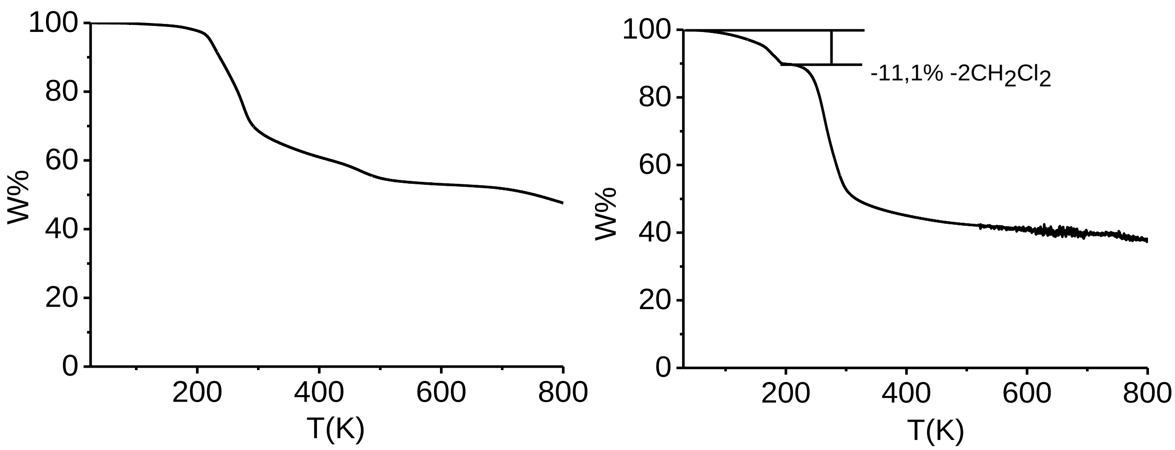

Fig. S2 TGA analysis for **1Dy** indicating no significant loss of solvent molecules before 200 0C and decomposition after 200 °C (left). TGA analysis for **2Dy** indicating loss of solvent molecules between RT and 200 °C and decomposition after 200 °C (right).

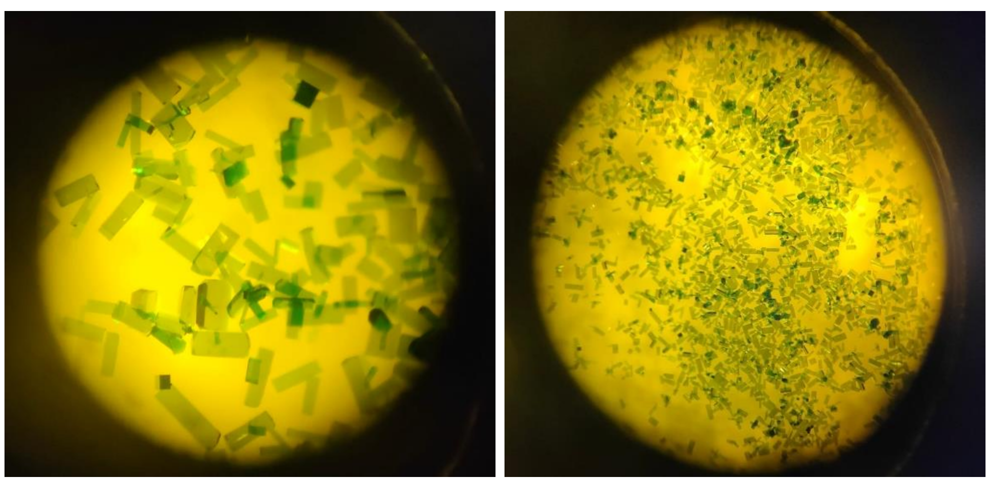

Fig. S3 Optical microscope images of **1Dy** in the mother liquor before filtration.

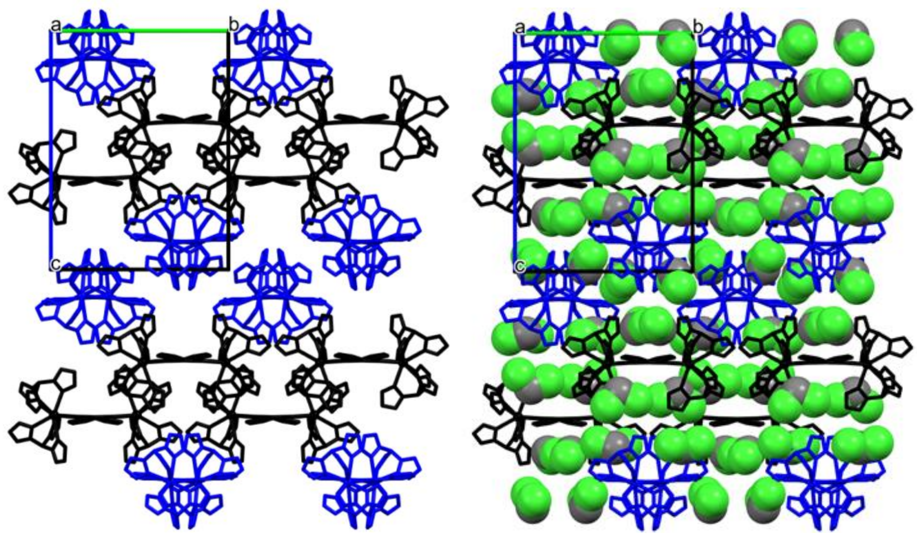

Fig. S4 Representation of the crystal packing along the *a* crystallographic axis for **1Dy**, without (left) and with (right) crystallization solvent molecules.

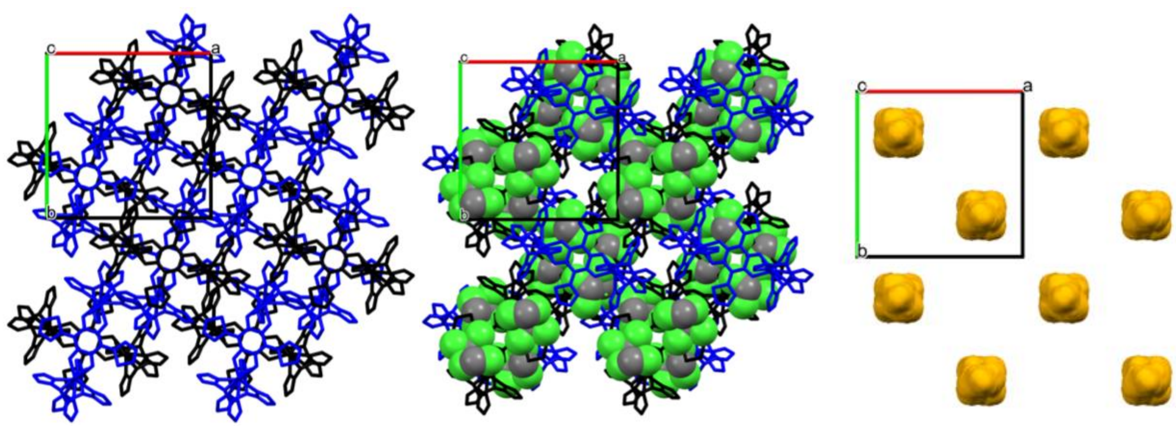

Fig. S5 Representation of the crystal packing along the *c* crystallographic axis for **1Dy** without (left) and with (middle) crystallization solvent molecules. Representation of voids filled by disordered water molecules (right).

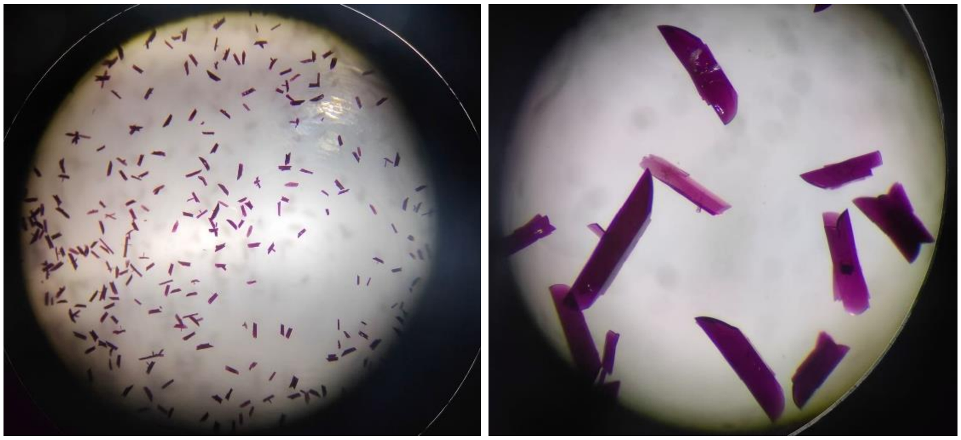

Fig. S6 Optical microscope images of **2Dy** in the mother liquor before filtration.

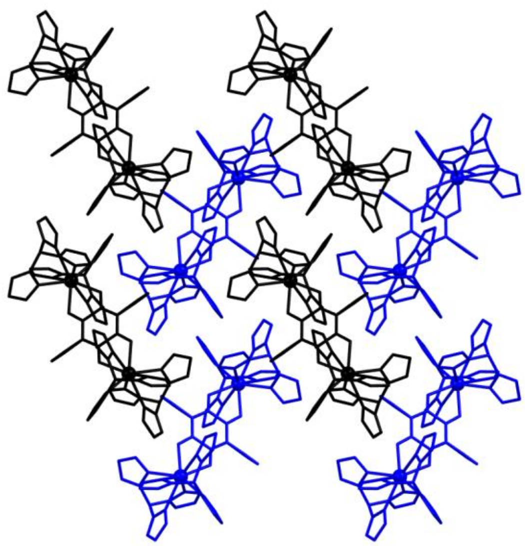

Fig. S7 Representation of the crystal packing along the *a* crystallographic axis for **2Dy**.

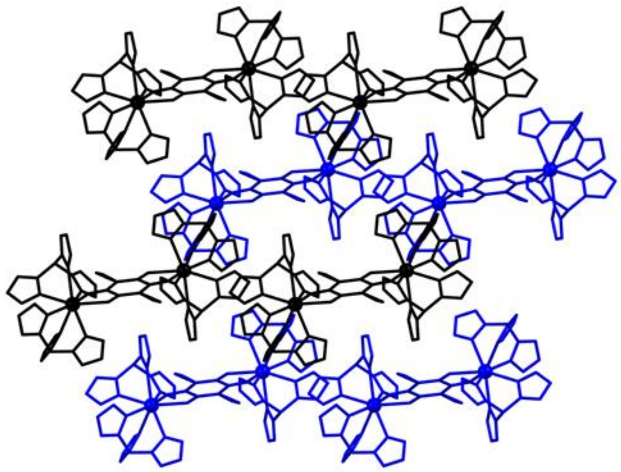

Fig. S8 Representation of the crystal packing along the *b* crystallographic axis for **2Dy**.

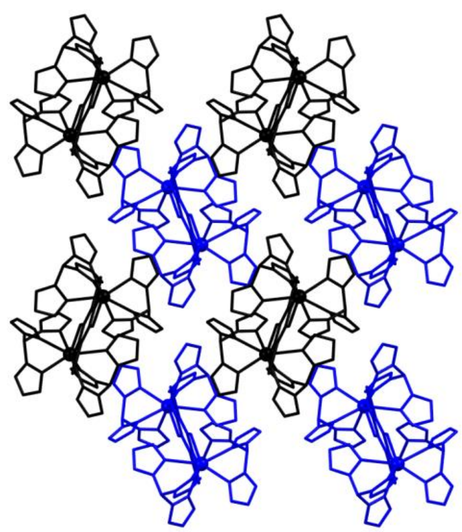

Fig. S9 Representation of the crystal packing along the *c* crystallographic axis for **2Dy**.

IR and UV-Vis spectroscopy

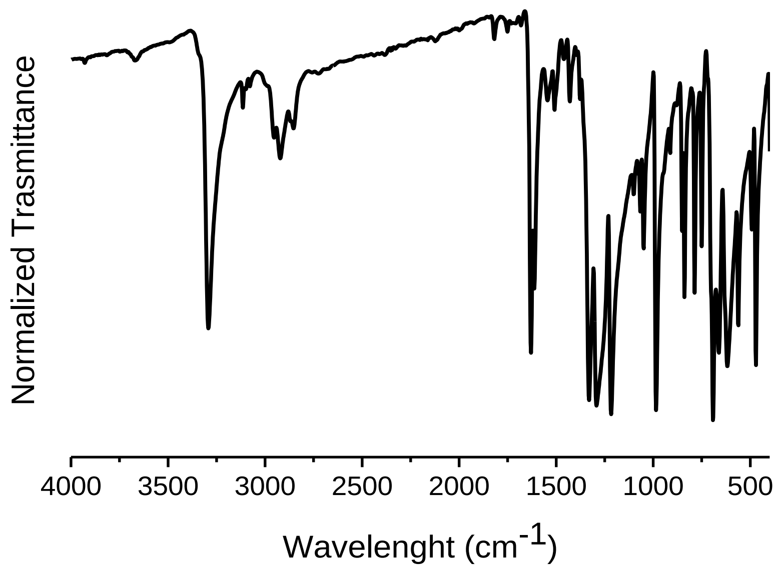

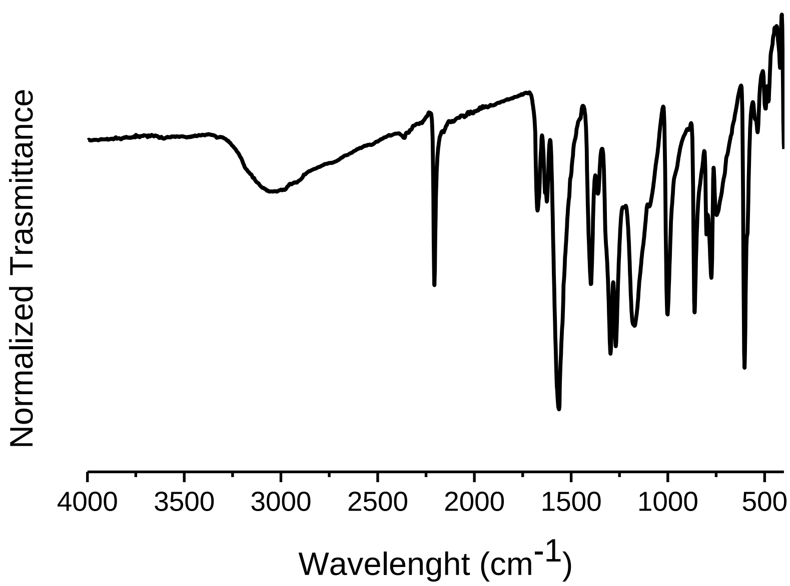

Fig. S10 FT-IR spectra for **Th_2An** (top) and for **KHClCNAn** (bottom).

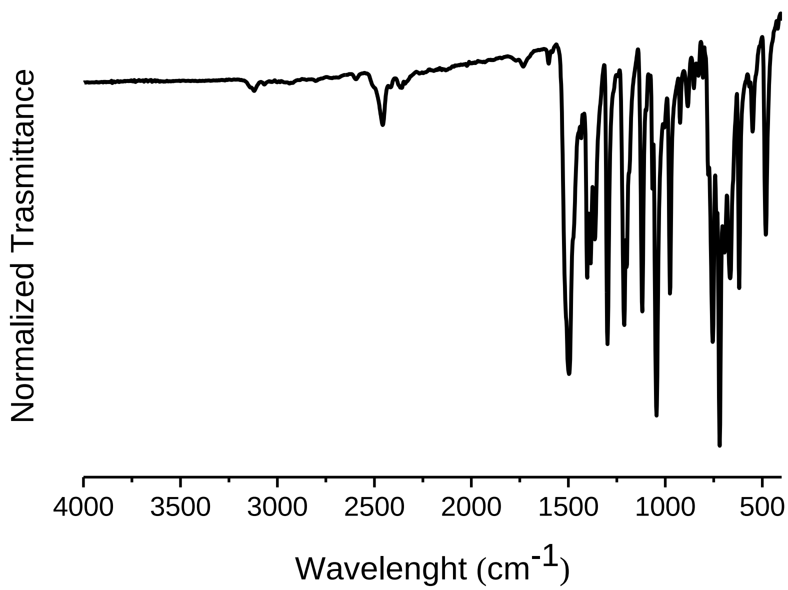

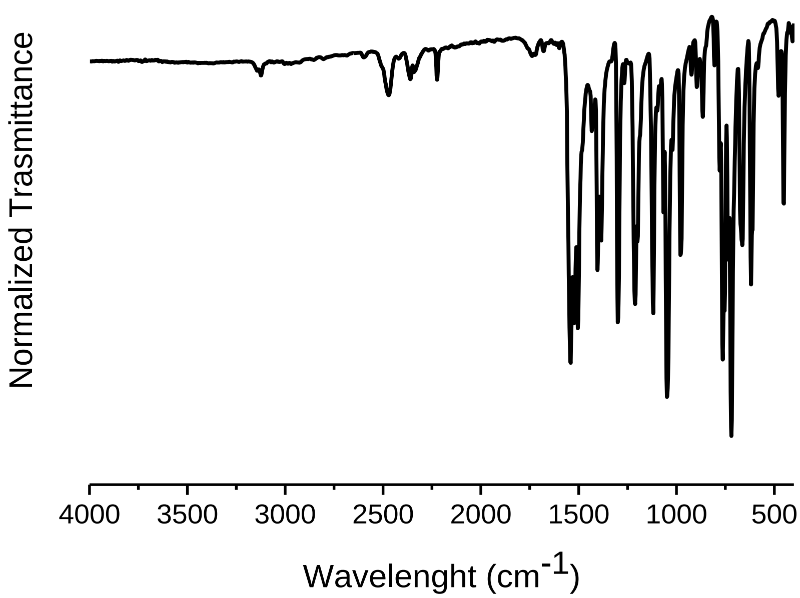

Fig. S11 FT-IR spectra for **1Dy** (top) and for **2Dy** (bottom).

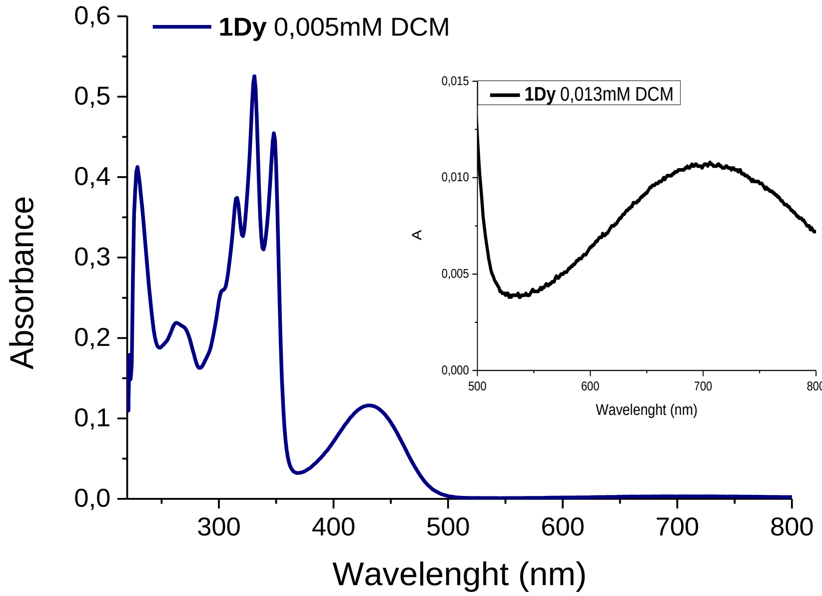

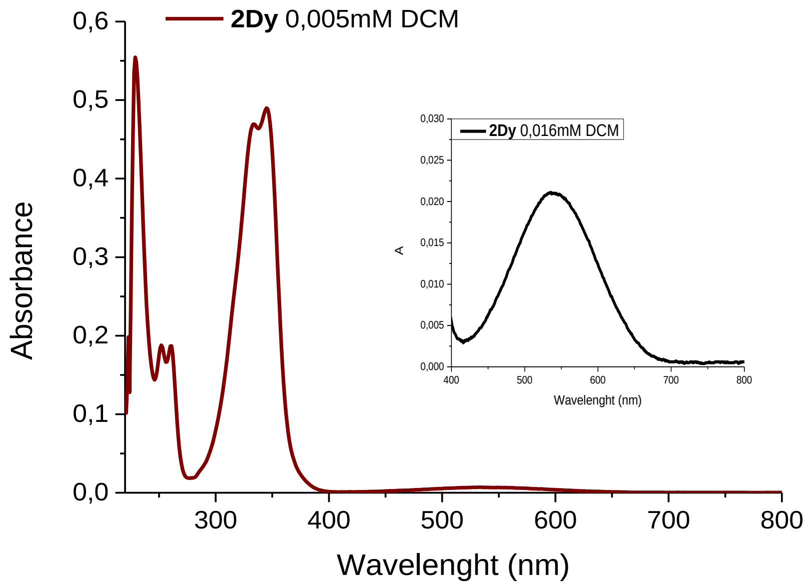

Fig. S12 UV-Vis absorption spectra in CH_2Cl_2 for **1Dy** (top) and for **2Dy** (bottom) between 220 nm and 800 nm. The inserts highlight the bands in the visible region with low extinction coefficients for more concentrated solutions.

Cyclic voltammetry measurements

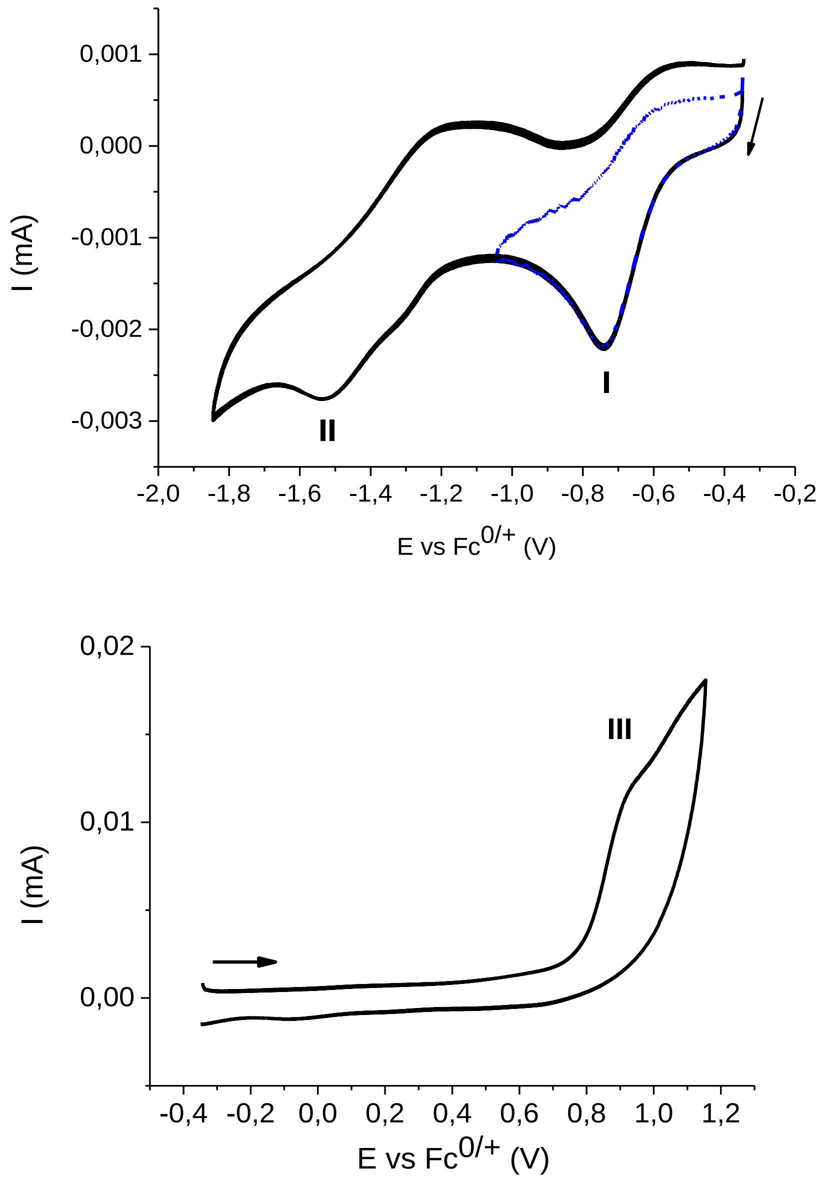

Fig. S13 Cyclic voltammogram for **H_2th_2An** in the cathodic region highlighting the two reduction processes (**I** & **II**); the dashed blue lines plot shows the voltammogram measured with a switching potential immediately past the first reduction to probe the irreversibility (top). Cyclic voltammogram for **H_2th_2An** in the anodic region highlighting the irreversible oxidation process (**III**) (bottom). Platinum disk 2 mm (WE), platinum wire (CE), Ag wire (RE), $TBAPF_6$ 0.25 M in CH_2Cl_2 as electrolyte and 0.005 M concentration. The arrows indicate the direction of forwarded scan, the voltammograms are referenced against the $Fc^{0/+}$ couple.

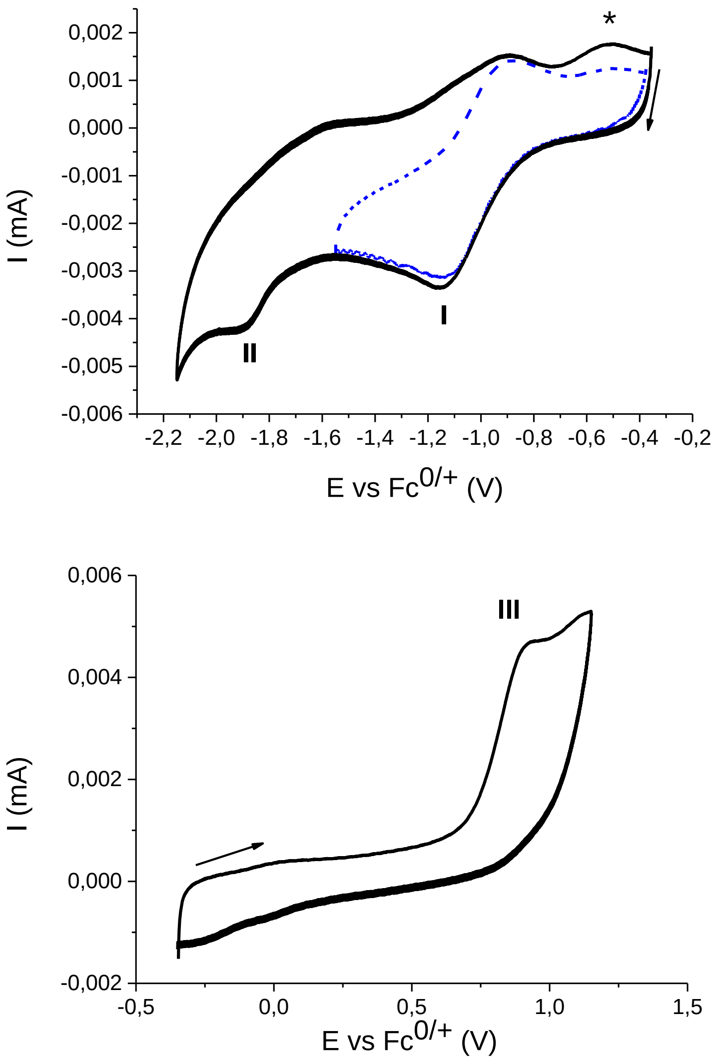

Fig. S14 Cyclic voltammogram for **KHClCNAn** in the cathodic region highlighting the two reduction processes (**I** & **II**); the dashed blue lines plot show the voltammogram measured with a switching potential immediately past the first reduction to probe the irreversibility (top). Cyclic voltammogram for **KHClCNAn** in the anodic region highlighting the irreversible oxidation process (**III**) (bottom). Platinum disk 2 mm (WE), platinum wire (CE), Ag wire (RE), $TBAPF_6$ 0.25 M in CH_3CN as electrolyte and 0.005 M concentration. The arrows indicate the direction of forwarded scan, the voltammograms are referenced against the $Fc^{0/+}$ couple.

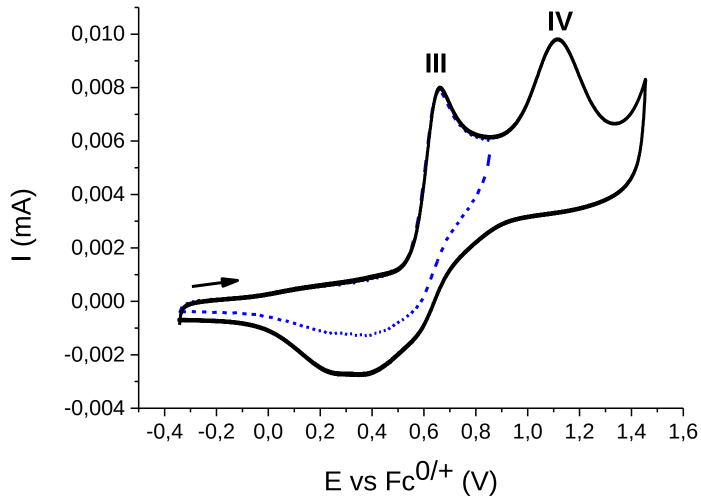

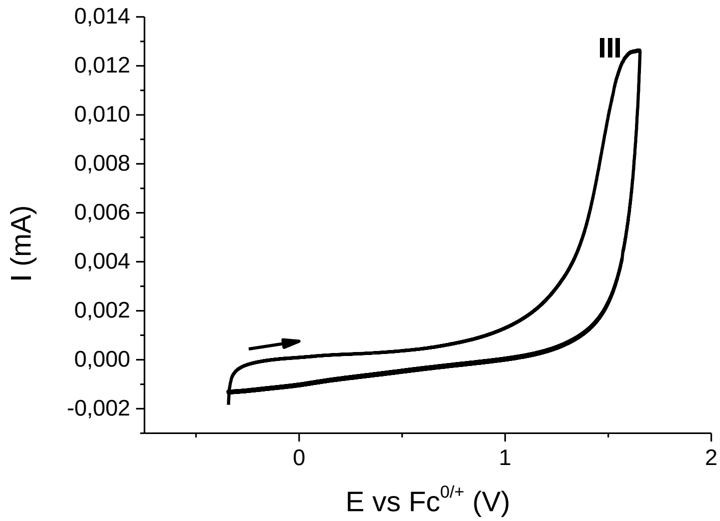

Fig. S15 Cyclic voltammogram for **1Dy** in the anodic region highlighting the two oxidation processes (**III** & **IV**); the dashed blue lines plot show the voltammogram measured with a switching potential immediately past the first oxidation to probe the irreversibility (top). Cyclic voltammogram for **2Dy** in the anodic region highlighting the irreversible oxidation process (**III**) (bottom). Platinum disk 2 mm (WE), platinum wire (CE), Ag wire (RE), $TBAPF_6$ 0.25 M in CH_2Cl_2 as electrolyte and 0.005 M complex concentration. The arrows indicate the direction of forwarded scan, the voltammograms are referenced against the $Fc^{0/+}$ couple.

Magnetic measurements

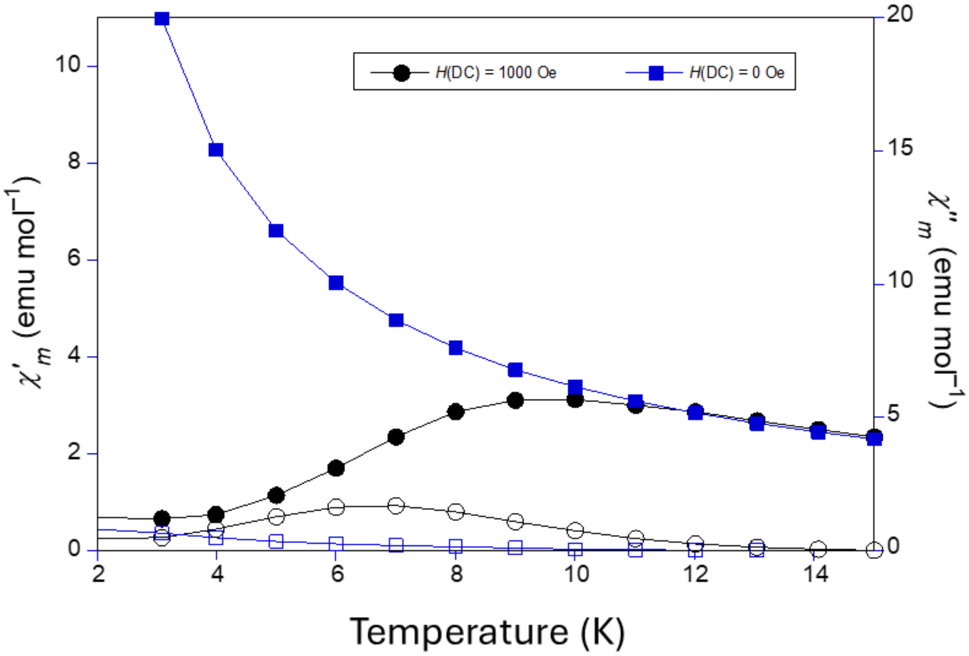

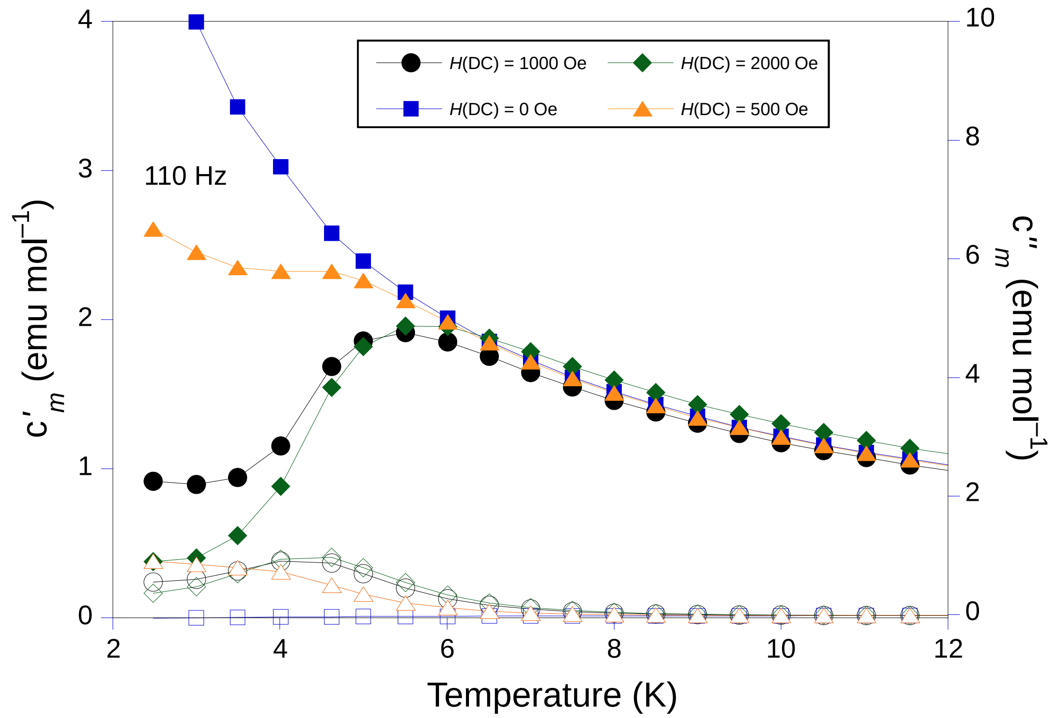

Fig. S16 Field dependence of the in-phase (top curves) and out-of-phase (bottom curves) ac magnetic susceptibility as a function of temperature for **1Dy** (top) and **2Dy** (bottom).

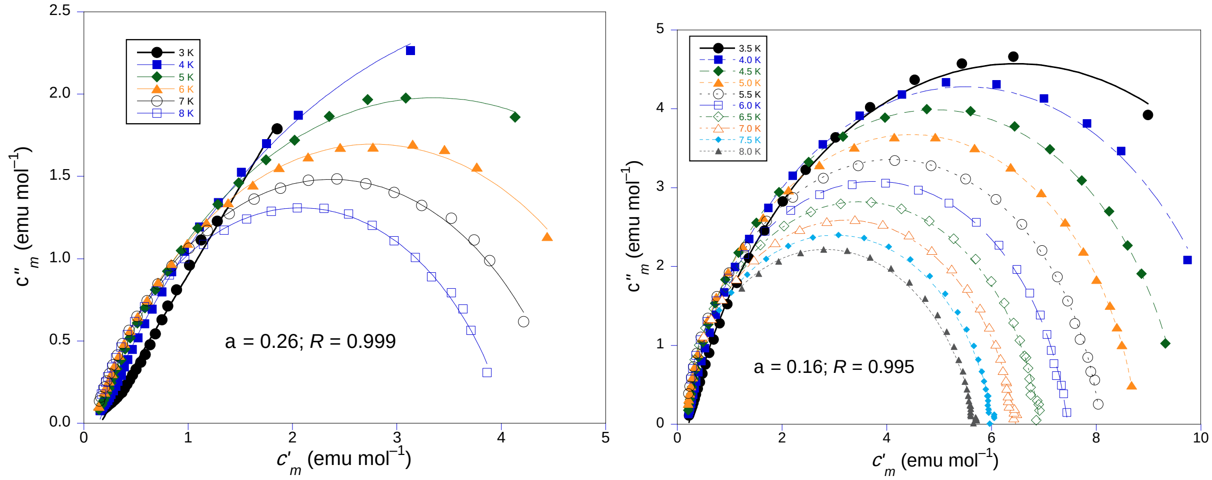

Fig. S17 Argand plots for **1Dy** (left) and **2Dy** (right).

NMR characterization

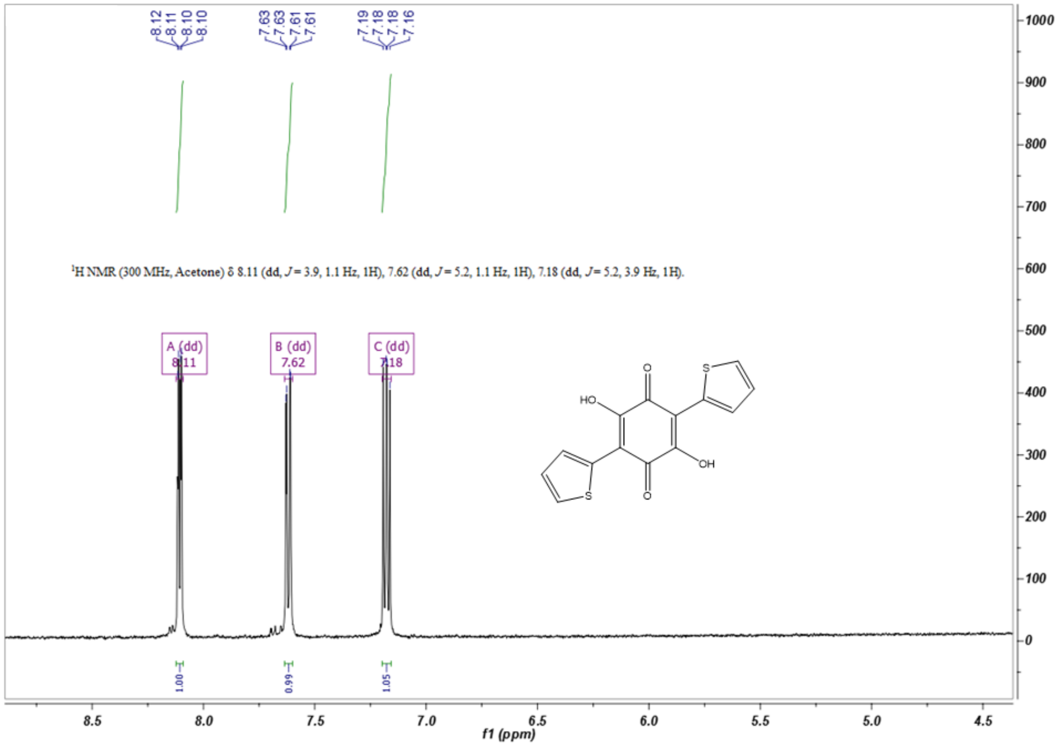

Fig. S18 ^{1}H-NMR spectrum for 2,5-dimethoxy-3,6-bis(thiophene-2-yl)-cyclohexa-2,5-diene-1,4-dione.

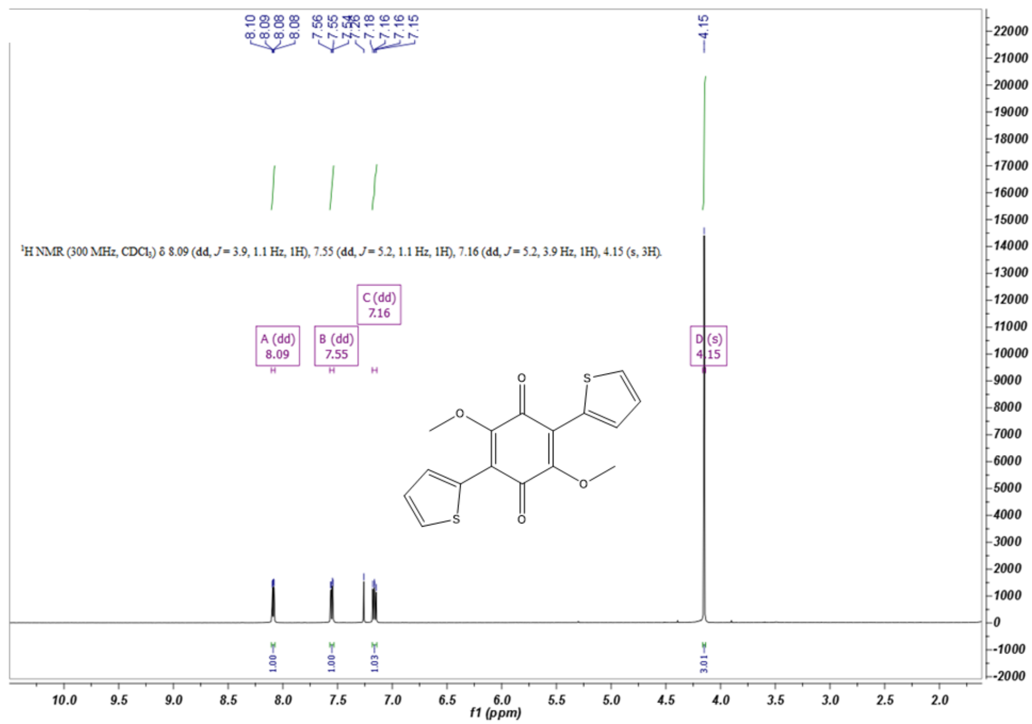

Fig. S19 ^{1}H-NMR spectrum for 2,5-dihydroxy-3,6-bis(thiophene-2-yl)-cyclohexa-2,5-diene-1,4-dione.

Quantum chemical calculations

Table S1 Computed energies levels (the ground state is set at zero), component values of the Lande *g* factor and wavefunction composition for each M_J state of the ground-state multiplet for Dy1 center in **1Dy**.

	E (cm^{-1})	g_x	g_y	g_z	WFT
1	0.0	0.0	0.0	19.8	0.99|±15/2⟩
2	118.8	0.5	0.8	17.2	0.75|±13/2⟩ + 0.12|±11/2⟩
3	151.7	2.8	3.5	12.4	0.36|±11/2⟩ + 0.23|±9/2⟩ + 0.20|±13/2⟩ + 0.09|±7/2⟩
4	170.6	2.9	6.1	12.0	0.19|±7/2⟩ + 0.18|±11/2⟩ + 0.18|±9/2⟩ + 0.15|±3/2⟩ + 0.15|±1/2⟩ + 0.13|±5/2⟩
5	191.5	1.1	1.4	15.8	0.23|±9/2⟩ + 0.22|±11/2⟩ + 0.20|±7/2⟩ + 0.13|±5/2⟩ + 0.13|±1/2⟩
6	241.1	0.2	0.5	15.7	0.33|±7/2⟩ + 0.30|±5/2⟩ + 0.21|±9/2⟩
7	259.3	0.3	0.6	18.3	0.36|±3/2⟩ + 0.25|±1/2⟩ + 0.22|±5/2⟩
8	609.3	0.0	0.0	19.9	0.40|±1/2⟩ + 0.30|±3/2⟩ + 0.17|±5/2⟩ + 0.08|±7/2⟩

Table S2 Computed energies levels (the ground state is set at zero), component values of the Lande *g* factor and wavefunction composition for each M_J state of the ground-state multiplet for Dy2 center in **1Dy**.

	E (cm^{-1})	g_x	g_y	g_z	WFT
1	0.0	0.0	0.0	19.8	0.99|±15/2⟩
2	119.0	0.5	0.7	17.1	0.76|±13/2⟩ + 0.12|±11/2⟩
3	153.0	2.7	3.6	12.6	0.38|±11/2⟩ + 0.23|±9/2⟩ + 0.19|±13/2⟩ + 0.09|±7/2⟩
4	173.9	2.7	6.5	11.4	0.21|±11/2⟩ + 0.21|±9/2⟩ + 0.19|±7/2⟩ + 0.14|±3/2⟩ + 0.13|±1/2⟩ + 0.11|±5/2⟩
5	192.6	1.5	1.6	15.9	0.22|±9/2⟩ + 0.22|±7/2⟩ + 0.18|±11/2⟩ + 0.15|±1/2⟩ + 0.14|±5/2⟩ + 0.09|±3/2⟩
6	243.2	0.2	0.6	15.2	0.34|±7/2⟩ + 0.30|±5/2⟩ + 0.22|±9/2⟩
7	261.5	0.3	0.7	17.9	0.38|±3/2⟩ + 0.24|±1/2⟩ + 0.22|±5/2⟩
8	612.0	0.0	0.0	19.9	0.40|±1/2⟩ + 0.30|±3/2⟩ + 0.17|±5/2⟩ + 0.08|±7/2⟩

Table S3 Computed energies levels (the ground state is set at zero), component values of the Lande *g* factor and wavefunction composition for each M_J state of the ground-state multiplet for Dy1 center in **2Dy**.

	E (cm^{-1})	g_x	g_y	g_z	WFT
1	0.0	0.1	0.1	19.6	0.97|±15/2⟩
2	84.2	1.8	2.2	16.4	0.53|±13/2⟩ + 0.24|±11/2⟩
3	115.4	8.7	6.1	3.2	0.25|±9/2⟩ + 0.21|±13/2⟩ + 0.14|±5/2⟩ + 0.14|±1/2⟩ + 0.11|±3/2⟩ + 0.09|±11/2⟩
4	129.0	1.1	3.3	12.4	0.26|±11/2⟩ + 0.17|±7/2⟩ + 0.15|±3/2⟩ + 0.12|±9/2⟩ + 0.11|±5/2⟩ + 0.10|±11/2⟩
5	168.1	0.3	1.7	15.4	0.25|±1/2⟩ + 0.19|±7/2⟩ + 0.17|±9/2⟩ + 0.15|±3/2⟩ + 0.11|±5/2⟩ + 0.10|±11/2⟩
6	208.3	0.6	1.4	15.3	0.31|±5/2⟩ + 0.27|±7/2⟩ + 0.17|±3/2⟩ + 0.10|±9/2⟩
7	271.2	0.2	0.3	19.3	0.26|±9/2⟩ + 0.24|±11/2⟩ + 0.17|±7/2⟩ + 0.13|±5/2⟩ + 0.09|±3/2⟩
8	500.0	0.0	0.0	19.8	0.39|±1/2⟩ + 0.30|±3/2⟩ + 0.18|±5/2⟩ + 0.08|±7/2⟩

Table S4 Computed energies levels (the ground state is set at zero), component values of the Lande *g* factor and wavefunction composition for each M_J state of the ground-state multiplet for Dy2 center in **2Dy**.

	E (cm^{-1})	g_x	g_y	g_z	WFT
1	0.0	0.1	0.1	19.6	0.97|±15/2⟩
2	82.4	1.5	1.7	16.8	0.54|±13/2⟩ + 0.23|±11/2⟩
3	118.7	1.1	1.6	11.1	0.31|±9/2⟩ + 0.27|±13/2⟩ + 0.10|±3/2⟩ + 0.10|±1/2⟩ + 0.10|±5/2⟩
4	130.2	3.1	7.0	11.2	0.30|±11/2⟩ + 0.19|±7/2⟩ + 0.16|±3/2⟩ + 0.14|±5/2⟩ + 0.13|±1/2⟩
5	170.7	0.3	2.2	14.6	0.25|±1/2⟩ + 0.20|±7/2⟩ + 0.18|±9/2⟩ + 0.15|±3/2⟩ + 0.09|±5/2⟩ + 0.09|±11/2⟩
6	209.7	0.9	1.8	15.1	0.33|±5/2⟩ + 0.24|±7/2⟩ + 0.18|±3/2⟩ + 0.08|±9/2⟩
7	277.1	0.2	0.3	19.3	0.27|±9/2⟩ + 0.23|±11/2⟩ + 0.19|±7/2⟩ + 0.13|±5/2⟩ + 0.09|±3/2⟩
8	503.2	0.0	0.0	19.8	0.39|±1/2⟩ + 0.30|±3/2⟩ + 0.18|±5/2⟩ + 0.08|±7/2⟩

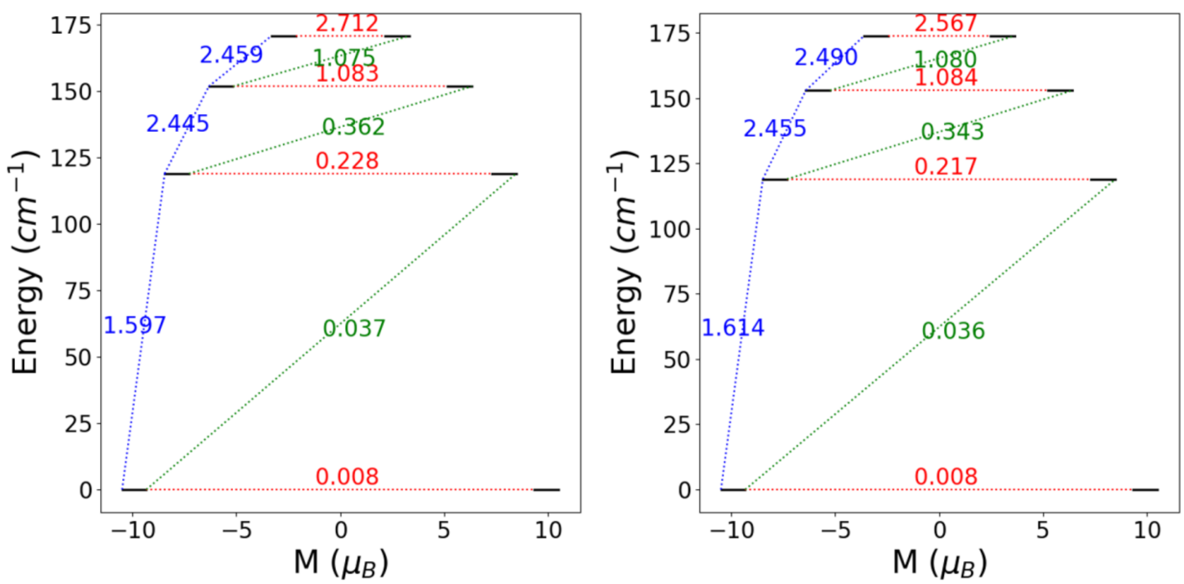

Fig. S20 Energies (in cm^{-1}) and projected μ_z (in µB) values along the ground magnetic axis for Dy1 (left) and Dy2 (right) of **1Dy**. Black lines represent the four lowest Kramers doublets. Values of the magnetic (i.e. isotropic Zeeman) transition moments between the states are given for comparison purpose. Values in red correspond to QTM (for the GS) and TA-QTM (for the ESs) mechanisms of the magnetization relaxation, whereas blue and green values correspond to Orbach mechanisms.

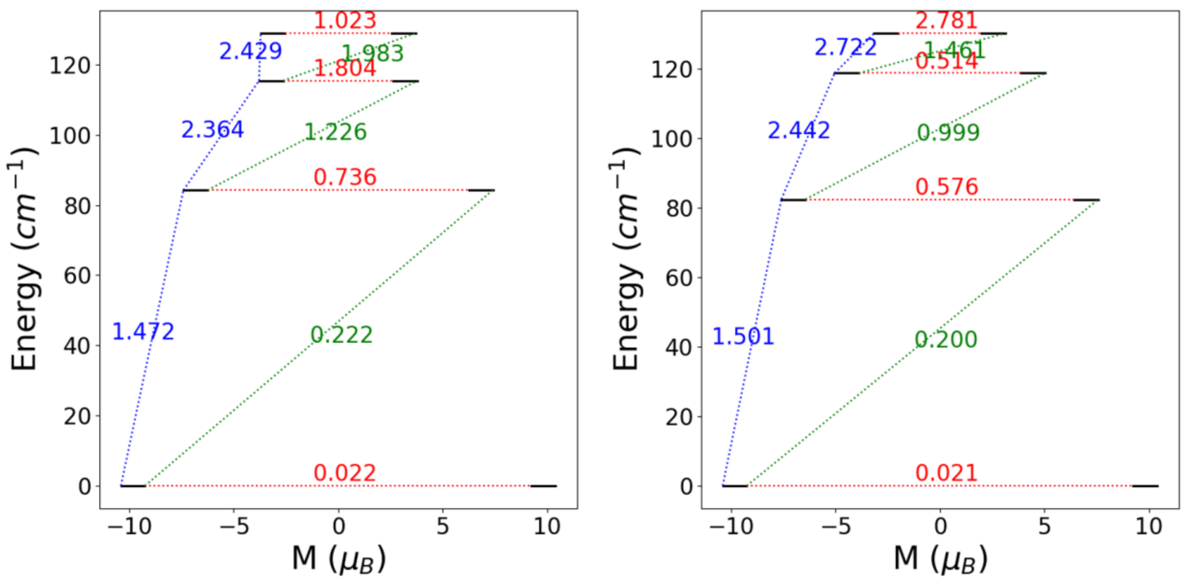

Fig. S21 Energies (in cm^{-1}) and projected μ_z (in μB) values along the ground magnetic axis for Dy1 (left) and Dy2 (right) of **2Dy**. Black lines represent the four lowest Kramers doublets. Values of the magnetic (i.e. isotropic Zeeman) transition moments between the states are given for comparison purpose. Values in red correspond to QTM (for the GS) and TA-QTM (for the ESs) mechanisms of the magnetization relaxation, whereas blue and green values correspond to Orbach mechanisms.

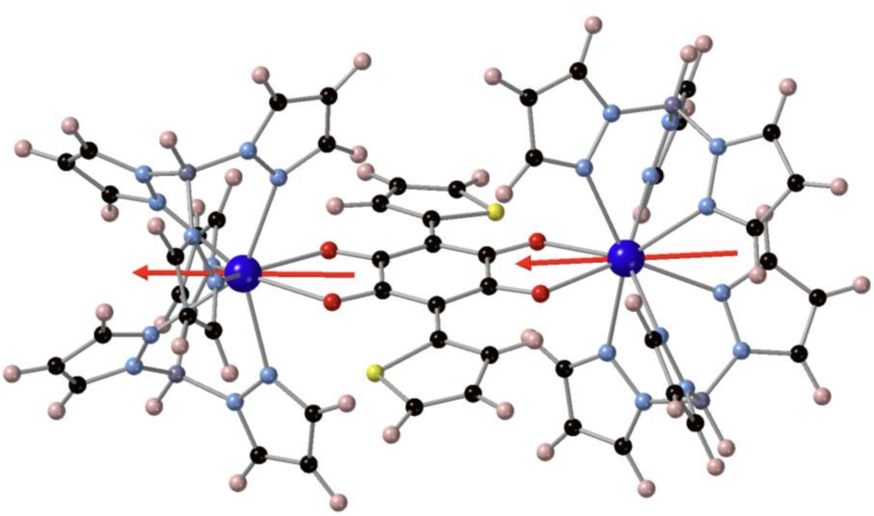

Fig. S22 Anisotropy axes of the Dy(III) ions in **1Dy**.

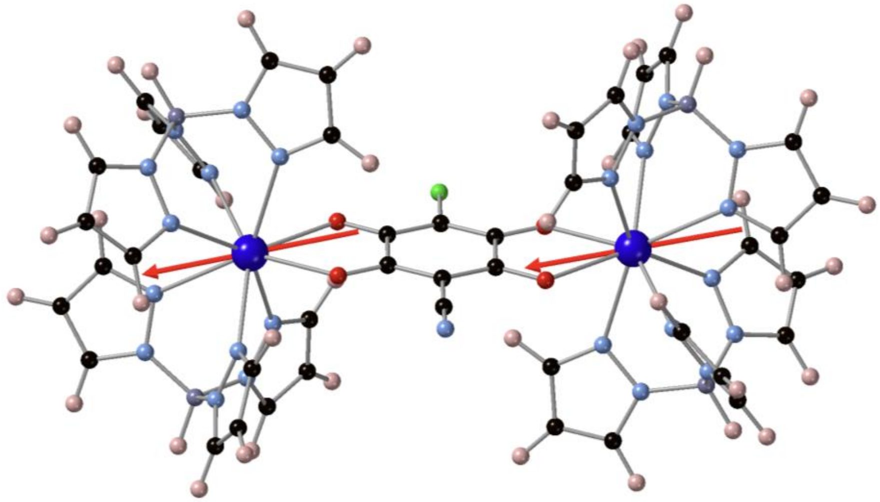

Fig. S23 Anisotropy axes of the Dy(III) ions in **2Dy**.

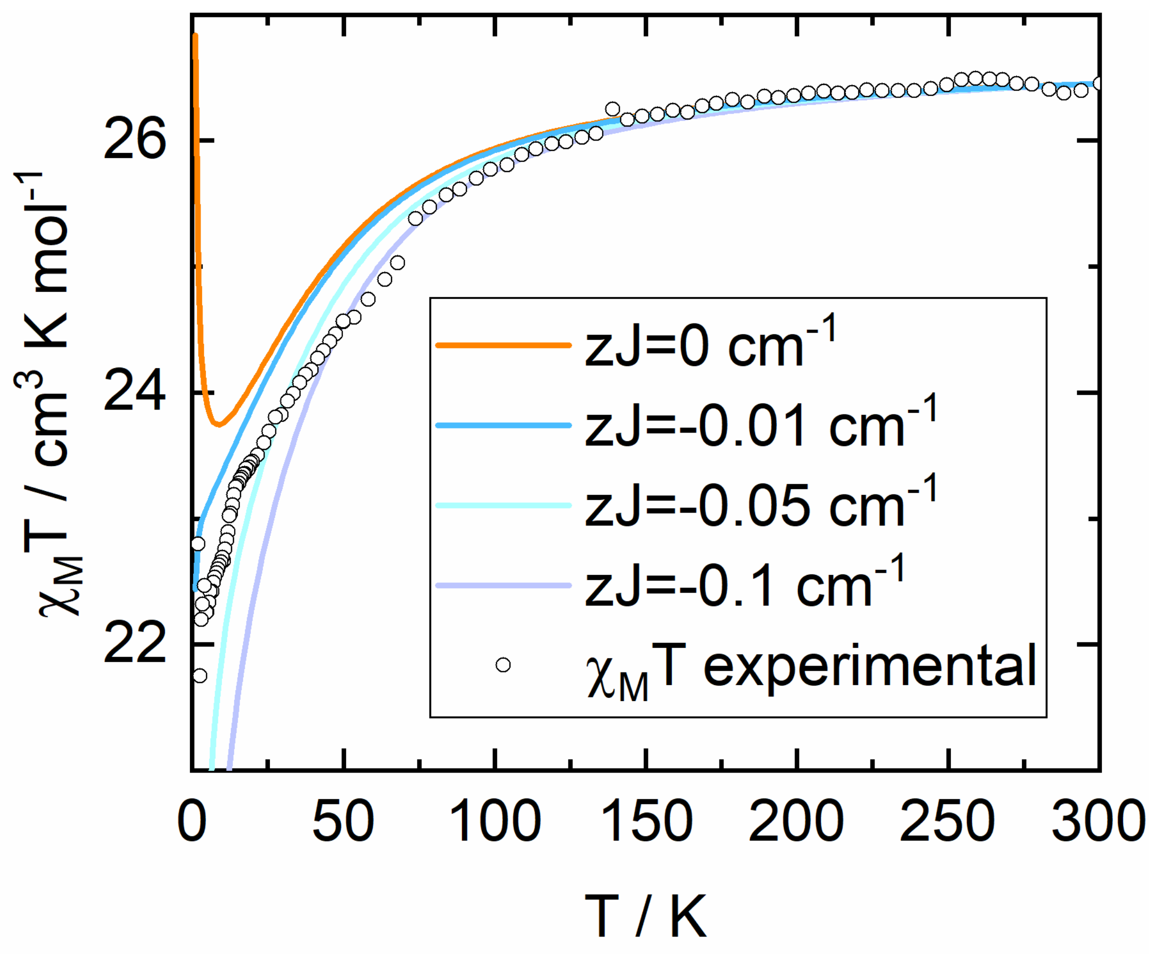

Fig. S24 Computed versus experimental thermal dependence of $\chi_m T$ for **2Dy**.